PHYSICAL REVIEW C **76**, 034305 (2007)

Neutron skin deduced from antiprotonic atom data

B. Alex Brown,[1,4] G. Shen,[2,3] G. C. Hillhouse,[2,4] J. Meng,[2,4,5,6] and A. Trzcińska[7]
[1]*Department of Physics and Astronomy, National Superconducting Cyclotron Laboratory, and Joint Institute for Nuclear Astrophysics, Michigan State University, East Lansing, Michigan 48824-1321, USA*
[2]*School of Physics, Peking University, Beijing 100871, People's Republic of China*
[3]*Department of Physics, Indiana University Bloomington, Indiana 47405, USA*
[4]*Department of Physics, University of Stellenbosch, Stellenbosch, South Africa*
[5]*Institute of Theoretical Physics, Chinese Academy of Science, Beijing 100080, People's Republic of China*
[6]*Center of Theoretical Nuclear Physics, National Laboratory of Heavy Ion Accelerator, Lanzhou 730000, People's Republic of China*
[7]*Heavy Ion Laboratory, Warsaw University, PL-02-093 Warsaw, Poland*

(Received 2 February 2006; revised manuscript received 29 June 2007; published 6 September 2007)

The relationship between the nucleon density at large radii and the value of the rms radius is investigated in the framework of Skyrme Hartree-Fock and relativistic mean-field models. From a comparison to the charge density we constrain the models in terms of the nuclear matter incompressibility and effective mass properties required to reproduce the density shape. The results are used to extract the rms neutron radius for ^{208}Pb from antiprotonic atom data. The result for the difference between the neutron and proton rms radii, the so-called neutron-skin thickness, is $S = 0.20(\pm 0.04)(\pm 0.05)$ fm, where ± 0.04 fm is experimental error from the antiprotonic line width, and ± 0.05 fm is the theoretical error suggested from the comparison of the models with the experimental charge density.

DOI: 10.1103/PhysRevC.76.034305 PACS number(s): 21.10.Gv, 21.60.Jz, 27.80.+w, 36.10.Gv

The neutron-skin thickness is defined by $S = R_n - R_p$ where R_n and R_p are the rms radii for point neutrons and protons, respectively. The neutron skin in heavy nuclei has been shown to be a unique measure of the density dependence of the neutron equation of state (EOS) near nuclear saturation density [1–3]. The density-dependent properties of the neutron EOS have a strong impact on the models of neutron stars [3–7]. Proton rms radii R_p for stable nuclei are determined at a high level accuracy from electron scattering and muonic atom data. The charge rms radius obtained for ^{208}Pb is $R_{ch} = 5.5013(7)$ fm [8], which gives $R_p = 5.45$ fm after taking into account the finite-size effects of the protons and neutrons [9]. Neutron rms radii are much more difficult to accurately determine. A model independent method of using the parity violating asymmetry in elastic scattering of electrons from ^{208}Pb to measure R_n to a 1% ($\pm$ 0.05 fm) accuracy is proposed for the PREX experiment at JLab [10]. There have been renewed attempts to obtain R_n from hadronic scattering data [11,12], but the error due to the many-body strong interaction effects is difficult to quantify [13]. A third method has been to use antiprotonic atom data to constrain the properties of the matter density at large radii [14]. In this article we will explore how the densities at large radii are related to nuclear matter properties and to the neutron rms radius.

A recent analysis of the x-ray cascade of antiprotonic atoms [15] has been carried out with zero-range and finite range models for the antiproton nucleus interactions. The analysis is based on two-parameter Fermi (2pF) shapes for the densities; $\rho(r) = \rho_0/[1 + \exp(r - c)/a]$. The proton density was fixed from the measured charge density using the 2pF shape fit obtianed by Fricke *et al.* [8] transformed to a 2pF shape for point-protons with the formula of Oset *et al.* [16]. Then a 2pF shape for neutrons was added. The matter density is the sum of the 2pF densities for protons and neutrons. In [15] equally good fits are obtained for a wide range of correlated c and a combinations for the neutron density with the resulting matter density curves shown in Fig. 1. The curves cross near $r = 9.8$ fm indicating that the antiprotonic atom data tightly constrain the matter near this effective radius. The annihilation probability distribution for antiprotonic atom has its average value near $r = 9$ fm (see Fig. 10 and Table VII of [15]). The value of $r = 9.8$ where the curves cross in Fig. 1 represents an effective radius for an average over the entire annihilation probability distribution. In addition, we find from Fig. 8 and Table VIII of [15] that the level width is nearly linearly proportional to the density at $r = 9.8$ fm. Thus the antiprotonic atom width of $\Gamma_{low} = 312(26)$ eV translated to a matter density of $\rho_m(r = 9.8 \text{ fm}) = 4.6(4) \times 10^{-4}$ nucleons/fm^3, and the antiprotonic atom width of $\Gamma_{up} = 5.9(8)$ eV translated to a matter density of $\rho_m(r = 9.8 \text{ fm}) = 4.6(6) \times 10^{-4}$ nucleon/fm^3. For comparison with theory we will use $\rho_m(r = 9.8 \text{ fm}) = 4.6(4) \times 10^{-4}$ nucleons/fm^3.

The curves in Fig. 1 have rms matter radii ranging from 5.60 to 6.04 fm. Thus, in the Fermi model the rms radius of the matter density cannot be determined unless a or c is constrained. In the early works [14,17,18] c was set equal to the proton-density value deduced from the charge density. In recent work [15] a range of c values were chosen from results from hadron scattering experiments together with additional information from a few Skyrme Hartree-Fock (SHF) and relativistic mean-field (RMF) models.

In this paper we show how the density distribution depends upon nuclear matter properties of the microscopic model. We use data for the charge density of ^{208}Pb to find the best models in terms of incompressibility and effective mass. Antiprotonic atom data can be used to extract the neutron rms radius in the framework of SHF and RMF models for the density. Our

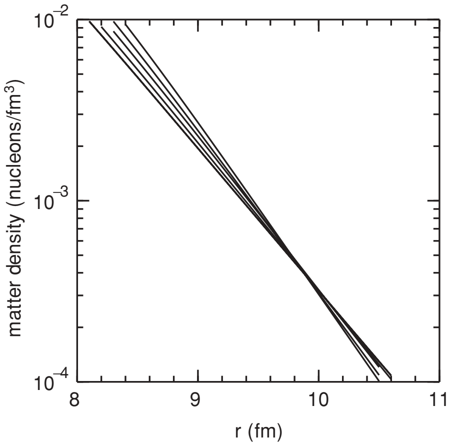

FIG. 1. Matter density distributions for ^{208}Pb obtained from Fermi-model shapes that reproduce the anti-proton x-ray data with the Batty optical potential.

approach does not use information from hadronic scattering experiments. We treat the SHF and RMF models for ^{208}Pb as different implementations of energy-density functional theory [19] for the spherical closed-shell single-Slater determinant configuration for ^{208}Pb. The parameter sets and references are given in Table I. The Skyrme Hartree-Fock parameter sets were based on those selected in Ref. [1] that passed the initial criteria for reproducing the binding energy difference between ^{100}Sn and ^{132}Sn and we add sly4 [20].

The SHF Skp [21] interaction provides an important variation in the nuclear matter properties with its incompressibility near $K = 200$ MeV and its effective mass of unity, but its mean-field properties are unstable [22]. Thus to replace Skp we have made a new SHF interaction called Skxs obtained from fitting the SHF parameters to the Skx data set [23], but with the constraint of $\alpha = 1/6$ for the density dependent potential (to give a small K value) and with a constraint to prevent the instability (this is done by constraining the neutron-matter effective mass to be near unity for all densities up to 10 times nuclear matter). Like Skx, it includes the scalar (RMF-type) form for the spin-orbit potential [23] and the addition of a charge-symmetry breaking potential to fit the ^{48}Ni-^{48}Ca binding energy difference [24]. The results are labeled by Skxsxx where xx is 100 times the neutron skin thickness in fm with the parameter values given in Table II.

TABLE I. Summary of the SHF and RMF models used in this work. Listed are neutron rms radius R_n , charge rms radius R_{ch} , the incompressibility K, and the Schröodinger effective mass m^*/m (the RMF values are from [25]). For the SHF models we give the power α for the density-dependence potential proportional to ρ^α.

Model	Ref.	R_n (fm)	R_{ch} (fm)	α	K (MeV)	m^*/m
TM1	[26]	5.754	5.541		280	0.71
nl3	[27]	5.740	5.505		270	0.67
nlsh	[28]	5.713	5.518		355	0.67
PK1s27	[29]	5.721	5.502		280	0.68
PK1s22	[29]	5.650	5.516		280	0.68
PK1s16	[29]	5.630	5.525		280	0.68
Skxs25	this work	5.700	5.503	1/6	200	0.97
Skxs20	this work	5.650	5.503	1/6	200	0.97
Skxs15	this work	5.600	5.503	1/6	200	0.97
Skx	[23]	5.607	5.498	1/2	270	0.99
Skxm	[23]	5.577	5.490	1/3	240	0.99
Skcs4	[30]	5.528	5.470	1/3	230	1
Sly4	[20]	5.614	5.506	1/6	230	0.69
Skt6	[31]	5.580	5.480	1/3	230	1
Mksa	[32]	5.616	5.490	0.719	350	0.76
Skm*	[33]	5.617	5.500	1/6	215	0.79
Skm	[34]	5.606	5.484	1/6	215	0.79
Ska	[35]	5.667	5.507	1	275	0.60
Sk4	[36]	5.647	5.507	1	320	0.46

TABLE II. The Skxs Skyrme parameters sets.

	Skxs15	Skxs20	Skxs25
t_0	−2883.29	−2885.24	−2887.81
t_1	291.60	302.73	315.50
t_2	−314.89	−323.42	−329.30
t_3	18239.55	18237.49	18229.81
x_0	0.4762	0.13746	−0.18594
x_1	−0.25433	−0.25548	−0.24766
x_2	−0.61109	−0.60744	−0.60119
x_3	0.52936	0.05428	−0.40902
W_0	161.35	162.73	163.93

For the RMF models, in addition to the nl3, nlsh, and TM1 models we include recent versions of PK1 [29] in which the RMF parameter Λ_v was adjusted to give different neutron rms radii [37]. The results are labeled by PK1sxx where xx is the 100 times the neutron skin thickness in fm for $\Lambda_v = 0.00$ (PK1s16), $\Lambda_v = 0.02$ (PK1s22), and $\Lambda_v = 0.04$ (PK1s27).

The charge density is obtained from the point proton and neutron densities obtained from the SHF and RMF calculations by folding them with the charge distributions of the proton and neutron as parameterized by Chandra and Sauer [38] that have an rms radius of 0.88 fm for the proton and a mean-square radius of -0.116 fm^2 for the neutron; these are close to the most recent Particle Data Group [9] values of 0.870(8) fm and $-0.1161(22)$, respectively. We also include the relativistic spin-orbit correction [39].

A feature of the mean-field models is that the density is built up in layers out of the shells that are filled. As an illustration of this we show in Fig. 2 the neutron density of ^{208}Pb obtained with the Skx Skyrme HF model [23] in terms of its contributions from the groups of filled orbitals. The neutron density at large radii is dominated by the single-particle density of the orbitals closest to the Fermi surface. In the bottom of Fig. 2 we show the percentage contribution to the total neutron density as a function of radius for the four ℓ values closest to the Fermi surface; each orbital has its own ℓ-dependent exponential fall off and as expected (due to the centrifugal barrier), for the largest radii the orbitals with low-ℓ values become dominant. The exponential fall off of each orbital is determined by its single-particle energy. The microscopic density has a shape that is more complicated than the Fermi distribution. In particular, in the Fermi-shape model

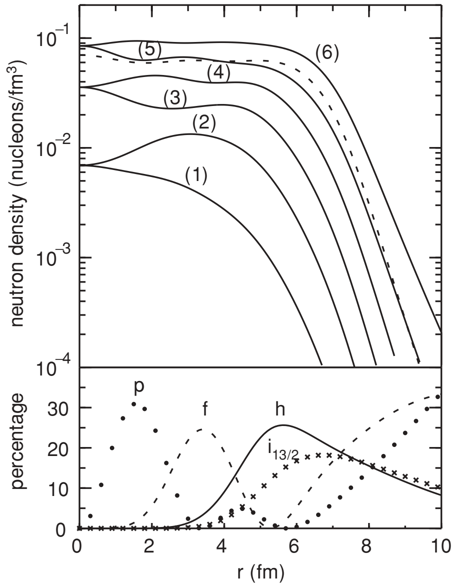

FIG. 2. Top: Density in nucleons/fm^3 vs the radius r in fm. The lines show the neutron density for the SHF Skx model in terms of a cumulative sums of neutron densities from the filled orbitals; from bottom to top: (1) = 0s [2 neutrons], (2) = (1) + 0p [6], (3) = (2) + 0d + 1s [12], (4) = (3) + 0f + 1p [20], (5) = (4) + 0g + 1d + 2s [30] and (6) = (5) + 0h + 1f + 2p + $\mathrm{i}_{13/2}$ [56]. The total proton density is shown by the dashed line. Bottom: the percentage contribution to the neutron density from the least bound neutron orbitals.

the exponential fall is fixed once the parameters c and a are fixed to an rms radius and diffuseness.

The experimental result for the matter density at $r = 9.8$ fm is [15] $\rho_m = 4.6(4) \times 10^{-4}$ nucleons/fm^3. Due to the Coulomb barrier the proton density falls off much faster than the neutron density (see Fig. 2). For Skm* the densities are $\rho_n(r = 9.8\ \text{fm}) = 3.11 \times 10^{-4}$ neutrons/fm^3 and $\rho_p(r = 9.8\ \text{fm}) = 0.50 \times 10^{-4}$ protons/fm^3. Thus, even with a 10% uncertainty in ρ_p we can reliably make a correction for the proton density and convert the antiprotonic matter density at $r = 9.8$ fm to a neutron density of $\rho_n(r = 9.8\ \text{fm}) = 4.1(4) \times 10^{-4}$ neutrons/fm^3. The ratio compared with the Skm* value of $\rho_n(r = 9.8\ \text{fm}) = 3.11 \times 10^{-4}$ neutrons/fm^3 is 1.32(13).

In the following we will show the densities from experiment and from various models divided by a common reference density. For guidance to the interpretation of the ratios we show in Fig. 3 results for the Fermi-shape density under the condition that the diffuseness is fixed (top) and under the condition that the rms radius is fixed (bottom). In the top we note that the asymptotic density changes by 20% from the relatively small change of 0.1 fm in the rms radius. This sensitivity of the asymptotic density to the rms radius allows the antiproton x-ray data with an line-width uncertainty of about 10% to have a high sensitivity to the rms radius. The bottom panel shows that the asymptotic density is also sensitive to the diffuseness for a fixed rms radius. This shows one aspect of the model dependence of extracting rms radii from the asymptotic density.

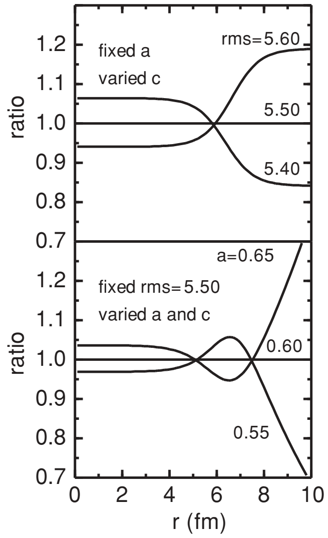

FIG. 3. Comparison of Fermi-shape densities with constraints on the diffuseness parameter (top) and on the rms radius (bottom).

The microscopic models can be tested in comparison to the relatively well-known charge density obtained from electron scattering. In Fig. 4 we show charge densities ratios relative to those of the Skm* SHF model. Skm* is chosen because it provides one of the best overall fits to the charge density [40]. The experimental charge densities (black) come from model independent analysis of electron scattering data and muonic atom data—min-max lines from [41,42], circles from [43], and crosses from [44]. The charge density is well constrained between $r = 2$ and $r = 8$ fm. The models are all relatively well constrained (fitted) to the experimental rms charge radius. In comparison with the bottom of Fig. 3 it is evident that the main difference between experiment and the models is the diffuseness with many of the models, including all of RMF models, having a diffuseness that is too small compared to the data. The diffuseness is strongly correlated with nuclear matter incompressibility given in Table I ranging from 320 MeV for Sk4 to 200 MeV for Skxsxx. Within the SHF models K is closely controlled by the power of the density-dependent potential, π^{α}, with $\alpha = 1$ for Sk4 down to and $\alpha = 1/6$ for Skxsxx.

Beyond the consideration of diffuseness (that shows up as in the bottom of Fig. 3 by the ratio crossing unity two times near the nuclear surface) there are deviations between the experiment and theory of higher order (associated with the ratios crossing the unity three times around the surface). This higher-order effect is relatively small up to $r = 8$ fm (with ratio deviations below 2% for Skm* and Skxsxx), but becomes enhanced at larger radii with a ratio (relative to Skm*) of 1.1 at $r = 9$ fm with an extrapolation to a ratio of 1.2 at $r = 10$ fm. The asymptotic dependence within the models is partly associated with the effective mass that range from $(m^*/m) = 0.46$ for Sk4 to $(m^*/m) = 1$ for Skx, Skxm, Skxsxx, Skcs4, and Skt6 (see Table I). Models with a relatively small effective mass have nucleon separation energies that are relatively large and hence densities that fall off relatively fast compared to the Skm* reference density. However, none of our

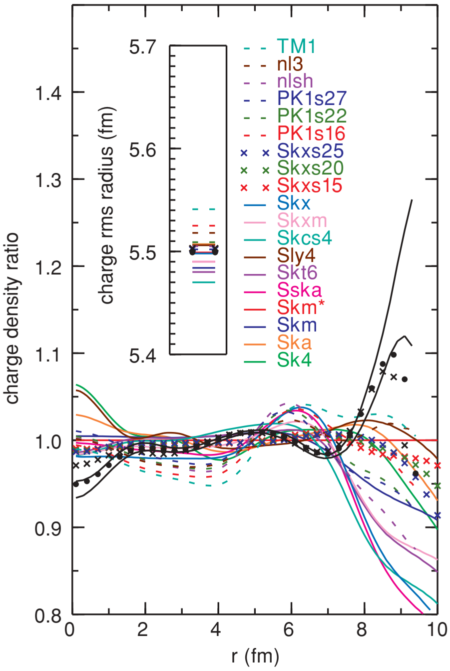

FIG. 4. (Color online) The charge densities from SHF (Skxsxx with crosses and the others with solid lines) and RMF (dashed lines) models normalized to the Skm* SHF The black points are those obtained from three analysis of electron scattering data. The rms charge radii shown in the inset.

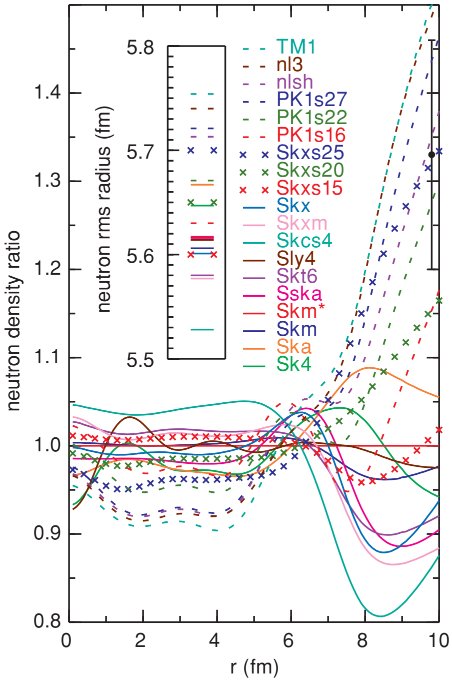

FIG. 5. (Color online) The neutron densities from SHF (Skxsxx with crosses and the others with solid lines) and RMF (dashed lines) models normalized to the Skm* SHF density. The black point at $r = 9.8$ fm is deduced from the anti-protonic x-ray data. The rms neutron radii are shown in the inset.

models can explain the 10% rise in the charge density at $r = 9$ fm.

We are now in a position to evaluate the neutron densities shown in Fig. 5 with the Skm* SHF model taken as the reference density. The value for the neutron density at $r = 9.8$ fm relative to Skm* is shown by the point with error bar. In the model ratios we can qualitatively observe the effects discussed previously; due to the change in rms radius (in analogy to the top part of Fig. 3), due to the change in the diffuseness (in analogy to the bottom part of Fig. 3) and the due to the change in slope of the density at large radii that is partly related to the effective mass. From the charge density comparison we chose the Skm*, Sly4, and Skxsxx SHF interactions as the best ones to use for the comparison to experiment. When these SHF models are interpolated to match the experimental point at $r = 9.8$ fm they all give the same interpolated neutron rms radius of $R_n = 5.70(4)$ fm. Thus with $R_p = 5.45$ fm the deduced neutron skin is $S = R_n - R_p = 0.25(4)$ fm. All models that give the best account of the charge-density give a consistent result for the neutron rms radius. However, even these best models under-predict the charge density by 20% at $r = 9.8$ fm radii. A factor of 1.2 corresponds to an apparent rms radius shift of 0.10 fm. Thus the charge density comparison suggests a correction of $-0.05(5)$ fm. In total we have $S = 0.20(\pm 0.04)(\pm 0.05)$ fm, where ± 0.04 fm is experimental error from the antiprotonic line width, and ± 0.05 fm is the theoretical error suggested from the comparison with the charge density.

In conclusion, microscopic models are required to connect the densities at large radii to rms radius. We find that those models with a small incompressibility of $K \approx 200$–220 MeV, and an effective mass near unity give the best reproduction of the measured charge density. In comparison with the charge density there is a higher-order effect missing in even the best models giving up to 2% deviation in the density inside of $r = 8$ fm and a 10% enhancement of experiment over theory in the asymptotic density near $r = 9$ fm where the density is about 10^{-3} of its interior value. Taking those models that best reproduce the charge density we obtain $S = R_n - R_p = 0.20(\pm 0.04)(\pm 0.05)$ fm, where ± 0.04 fm is experimental error from the antiprotonic line width, and $\pm$ 0.05 fm is the theoretical error suggested from the comparison of the models with the experimental charge density at $r = 9$ fm. This contains an empirical correction of $-0.05(\pm 0.05)$ fm. The correction could be removed if better microscopic models can be obtained in comparison to the charge density. Improved models may require the explicit addition of ground state correlations. Our results can be compared to values of $K = 248(9)$ MeV for the incompressibility and $S < 0.22$ fm for the neutron skin-thickness obtained from an RMF analysis of giant monopole and dipole resonances in ^{90}Zr and ^{208}Pb [13,45].

We thank Jerzy Jastrzębski for helpful comments on the paper. Support for this work was provided from U.S. National Science Foundation grant no. PHY-0555366, DOE Grant DE-FC02-07ER41457 and South African NRF grants GUN Nos. 2068517 (B.A.B.) and 2054166 (G.C.H.). This work is partly supported by the Major State Basic Research Development Program under contract no. G2000077407, the National Natural Science Foundation of China under grant 100435010 and 10221003.

[1] B. A. Brown, Phys. Rev. Lett. **85**, 5296 (2000).
[2] S. Typel and B. A. Brown, Phys. Rev. C **64**, 027302 (2001).
[3] C. J. Horowitz and J. Piekarewicz, Phys. Rev. Lett. **86**, 5647 (2001); Phys. Rev. C **64**, 062802(R) (2001); **66**, 055803 (2002).
[4] A. W. Steiner, M. Prakash, J. M. Lattimer, and P. J. Ellis, Phys. Rep. **411**, 325 (2005).
[5] J. Carriere, C. J. Horowitz, and J. Piekarewicz, Astrophys. J. **593**, 463 (2003).
[6] S. F. Ban, J. Li, S. Q. Zhang, H. Y. Jia, J. P. Sang, and J. Meng, Phys. Rev. C **69**, 045805 (2004).
[7] J. Meng, H. Toki, S. G. Zhou, S. Q. Zhang, W. H. Long, and L. S. Geng, Prog. Part. Nucl. Phys. **57**, 470 (2006).
[8] G. Fricke *et al.*, At. Data Nucl. Data Tables **60**, 177 (1995).
[9] S. Eidelman *et al.* (Particle Data Group), Phys. Lett. **B592**, 1 (2004).
[10] R. Michaels, P. A. Souder, and G. M. Urciouli, Thomas Jefferson National Accelerator Facility Proposal E-00-003, 2002, http://hallaweb.jlab.org/parity/prex/pbup2005.pdf
[11] S. Karataglidis, K. Amos, B. A. Brown, and P. K. Deb, Phys. Rev. C **65**, 044306 (2002).
[12] B. C. Clark, L. J. Kerr, and S. Hama, Phys. Rev. C **67**, 054605 (2003).
[13] J. Piekarewicz and S. P. Weppner, Nucl. Phys. **A778**, 10 (2006).
[14] A. Trzcińska, J. Jastrzębski, P. Lubiński, F. J. Hartmann, R. Schmidt, T. von Egidy, and B. Kłos, Phys. Rev. Lett. **87**, 082501 (2001).
[15] B. Klos *et al.*, Phys. Rev. C **76**, 014311 (2007).
[16] E. Oset, P. F. de Cordoba, L. L. Salcedo, and R. Brockmann, Phys. Rep. **188**, 79 (1990).
[17] P. Lubiński, J. Jastrzębski, A. Trzcińska, W. Kurcewicz, F. J. Hartmann, W. Schmid, T. von Egidy, R. Smolańczuk, and S. Wycech, Phys. Rev. C **57**, 2962 (1998); R. Schmidt *et al.*, *ibid.* **60**, 054309 (1999).
[18] J. Jastrzębski, A. Trzcińska, P. Lubiński, B. Kłos, F. J. Hartmann, T. von Egidy, and S. Wycech, Int. J. Mod. Phys. E **13**, 343 (2004).
[19] P. Hohenberg and W. Kohn, Phys. Rev. **136**, B864 (1964); W. Kohn and L. J. Sham, Phys. Rev. **140**, A1133 (1965).
[20] E. Chabanat, P. Bonche, P. Haensel, J. Meyer, and T. Schaeffer, Nucl. Phys. **A635**, 231 (1998).
[21] J. Dobaczewski, H. Flocard, and J. Treiner, Nucl. Phys. **A422**, 103 (1984).
[22] T. Lesinski, K. Bennaceur, T. Duguet, and J. Meyer, Phys. Rev. C **74**, 044315 (2006).
[23] B. A. Brown, Phys. Rev. C **58**, 220 (1998).
[24] B. A. Brown, W. A. Richter, and R. Lindsay, Phys. Lett. **B483**, 49 (2000).
[25] W. H. Long, Nguyen Van Giai, and Jie Meng, Phys. Lett. **B640**, 150 (2006).
[26] Y. Sugahara and H. Toki, Nucl. Phys. **A578**, 557 (1994).
[27] G. A. Lalazissis, J. König, and P. Ring, Phys. Rev. C **55**, 540 (1997).
[28] M. M. Sharma, M. A. Nagarajan, and P. Ring, Phys. Lett. **B312**, 377 (1993).
[29] W. H. Long, J. Meng, N. Van Giai, and S. G. Zhou, Phys. Rev. C **69**, 034319 (2004).
[30] Y. Aboussir, J. M. Pearson, A. K. Dutta, and F. Tondeur, At. Data Nucl. Data Tables **61**, 127 (1995).
[31] F. Tondeur, M. Brack, M. Farine, and J. M. Pearson, Nucl. Phys. **A420**, 297 (1984).
[32] M. M. Sharma, G. Lalazissis, J. Konig, and P. Ring, Phys. Rev. Lett. **74**, 3744 (1995).
[33] J. Bartel, P. Quentin, M. Brack, C. Guet, and M. B. Hakansson, Nucl. Phys. **A386**, 79 (1982).
[34] H. Krivine, J. Treiner, and O. Bohigas, Nucl. Phys. **A336**, 155 (1980).
[35] H. S. Kohler, Nucl. Phys. **A257**, 301 (1976).
[36] M. Beiner, H. Flocard, and N. van Giai, Nucl. Phys. **A238**, 29 (1975).
[37] G. Shen, J. Li, G. C. Hillhouse, and J. Meng, Phys. Rev. C **71**, 015802 (2005); erratum under preparation.
[38] H. Chandra and G. Sauer, Phys. Rev. C **13**, 245 (1976).
[39] W. Bertozzi, J. Friar, J. Heisenberg, and J. W. Negele, Phys. Lett. **B41**, 408 (1972).
[40] W. A. Richter and B. A. Brown, Phys. Rev. C **67**, 034317 (2003).
[41] I. Sick, Nucl. Phys. **A218**, 509 (1974).
[42] B. A. Brown, S. E. Massen, J. I. Escudero, P. E. Hodgson, G. Madurga, and J. Vinas, J. Phys. G **9**, 423 (1983).
[43] H. Euteneuer, J. Friedrich, and N. Vögler, Nucl. Phys. **A298**, 452 (1978).
[44] J. L. Friar, J. Heisenberg, and J. W. Negele, in Proceedings of the June Workshop in Intermediate Energy Electromagnetic Interactions, edited by A. M. Bernstein, Massachusetts Institute of Technology (1977), p. 325.
[45] B. G. Todd-Rutel, J. Piekarewicz, Phys. Rev. Lett. **95**, 122501 (2005).